CHALMERS
UNIVERSITY OF TECHNOLOGY

Numerical Modeling of Dynamic Thermal Coupling in GaN HEMTs Calibrated by Transient Measurements

Citation for the original published paper (version of record):
Kristensen, T., Nilsson, T., Divinyi, A. et al (2024). Numerical Modeling of Dynamic Thermal Coupling in GaN HEMTs Calibrated by Transient Measurements. IEEE Transactions on Electron Devices, In Press. http://dx.doi.org/10.1109/TED.2024.3478180

Numerical Modeling of Dynamic Thermal Coupling in GaN HEMTs Calibrated by Transient Measurements

Tobias Kristensen, *Graduate Student Member, IEEE,* Torbjörn M. J. Nilsson, *Member, IEEE,* Andreas Divinyi, Johan Bremer, and Mattias Thorsell, *Member, IEEE*.

***Abstract*— The dynamic thermal coupling within GaN HEMTs is characterized and modeled in a FEM solver to determine the thermal impedance of the HEMT. The study presents a method for calibrating the FEM model based on transient measurements with integrated temperature sensors placed 7.5, 91.5, and 175.5 µm away from a heat source. A sensitivity analysis is presented to show that the influence of the epitaxial layers, substrate, and die-attach layer can be differentiated. The method is used to calibrate a model that accurately replicates the measured thermal coupling. The model is assessed for different baseplate temperatures and a time-varying signal. Finally, an example is presented to show how thermal coupling changes the thermal impedance of GaN HEMTs and how the results can be used for layout optimization. The presented model and calibration method can also be used to evaluate how the device's packaging influences its thermal impedance.**

***Index Terms*— Electro-thermal device modeling, gallium nitride, time-varying systems.**

I. Introduction

THE growing interest in active antenna array systems for communication and remote sensing applications demands devices that reliably can deliver high power densities at high-frequencies and elevated temperatures. The wide bandgap and high electron mobility of the Gallium Nitride (GaN) High Electron Mobility Transistors (HEMT) make it an excellent solution for these applications. However, high power density makes self-heating effects an instrumental part of the device performance of the GaN HEMTs due to thermal resistances in the epitaxial layers, substrate, and package. This self-heating plays a role in the dynamic behavior of the HEMT as a source of time-variance and memory effects that can impact, e.g., the linearity of the device [1]-[4]. Therefore, it is important to model dynamic self-heating in a GaN HEMT.

The dynamic self-heating is predominantly an intrinsic effect in the GaN HEMT channel for the initial 100 ns after a change in dissipated power [5], [6]. The heat generation spreads out of the channel beyond 100 ns and affects the neighboring channels in an HEMT [7]-[10]. This thermal coupling increases the HEMTs thermal impedance and makes it layout-dependent [11]. Finite Element Method (FEM) simulations are an important tool to efficiently model both intrinsic and extrinsic effects that influence the dynamic self-heating [12]. However, there is uncertainty related to the correct implementation of model parameters in a FEM simulation [11], [13]. Therefore, FEM simulations should be calibrated based on experimental results. FEM simulations are often calibrated based on experimental results for multichannel transistors. These experiments capture several effects at the same time, and it is challenging to isolate the effect of thermal coupling to ensure that it is correctly accounted for in a FEM model. Hence, it is interesting to investigate methods for characterizing the thermal coupling by itself and its use for calibration of FEM models.

This article investigates FEM modeling of dynamic thermal coupling in GaN HEMTs and presents a calibration method for uncertain model parameters. Experimental results are obtained from electrical transient measurements on a sensor integrated close to a heat source [14]-[16]. These measurements do not need optical access and can be used for the thermal characterization of packaged devices [16]. The separation between the sensor and the heat source allows accurate characterization of the thermal coupling. Further, looking at the step response and varying the separation from the heat source can be used to differentiate the influence of material parameters for the calibration of a FEM model. A calibrated FEM model is presented that accurately replicates the experimental results for different ambient temperatures and a time-varying signal. Finally, how this can be used for thermal optimization of device layouts is discussed.

II. Experimental setup

The test structure in Fig. 1 (a) is designed to measure the thermal coupling from a heat source to an integrated temperature sensor [14], [15]. The temperature sensor is realized as a 2.5 x 10 µm semiconductor resistor utilizing the

Manuscript received September 13, 2024. This work, conducted within the Advanced Digitalization program at the WiTECH Centre's REMU project, has been financed by VINNOVA, Chalmers University of Technology, Ericsson AB, Kongsberg AS, Saab AB, and United Monolithic Semiconductor. *(Corresponding author: Tobias Kristensen)*

T. Kristensen and J. Bremer are with the Microwave Electronics Laboratory, Department of Microtechnology and Nanoscience, Chalmers University of Technology, 412 96 Gothenburg, Sweden. (e-mail: tobias.kristensen@chalmers.se and bremerj@chalmers.se.)

T. M. J. Nilsson and A. Divinyi are with Saab AB, 412 89 Gothenburg, Sweden. (e-mail: torbjorn.mj.nilsson@saabgroup.com and andreas.divinyi3@saabgroup.com.)

M. Thorsell is with the Microwave Electronics Laboratory, Department of Microtechnology and Nanoscience, Chalmers University of Technology, 412 96 Gothenburg, Sweden, and Saab AB, 412 89 Gothenburg, Sweden. (e-mail: mattias.thorsell@chalmers.se.)

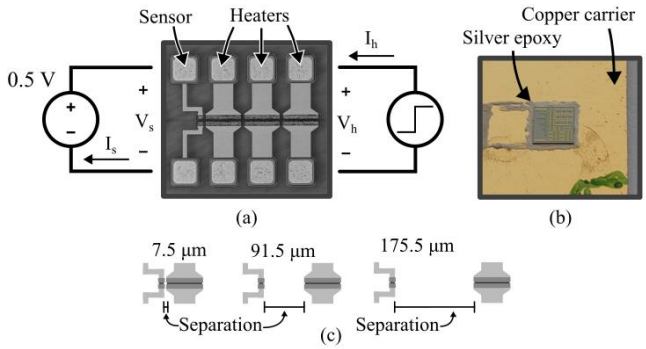

Fig. 1. Test structure shown in (a) with simplified schematic of measurement setup. (b) Mounted die. (c) Illustration of how the separation between the heater and sensor is defined.

strongly temperature-dependent sheet resistivity in the GaN channel [14], [16]. The heaters are realized as 2.5 µm x 75 µm semiconductor resistors. These heaters are ungated HEMTs, where removing the gate gives a simple and uniform source of heat dissipation in the channel without the influence of vertical electrical fields from the gate [17]. This allows for a more certain characterization of the thermal coupling, as the material parameters that govern the heat spreading away from the HEMT are the same for a gated and ungated device outside the channel. The heaters are placed with 7.5, 91.5, and 175.5 µm separation between the edge of the heater channel and the sensor channel, as illustrated in Fig. 1 (c). The test structure is manufactured in WIN Semiconductors NP15 GaN-on-SiC technology and mounted on a gold-sputtered copper carrier with a silver epoxy (Ablebond 84-1LMINB1), as shown in Fig. 1 (b). The baseplate temperature of the device is controlled by placing the heat spreader on a thermal chuck during the measurements. The heater and sensors are contacted with separate two-finger ground-signal (GS) probes (MPI T26P) together with short coaxial cables to minimize the parasitic inductances.

The sensor's IV characteristics are first measured at steady-state temperatures between 40°C and 200°C in Fig. 2 (b). Based on this, the steady state temperature (T_{Chuck}) is plotted against the sensor current (I_s) extracted at a bias voltage (V_s) of 0.5 V in Fig. 2 (a). The bias voltage of 0.5 V is chosen as a compromise between good temperature sensitivity and minimizing the influence of self-heating and potential electron-trapping in the sensor [14]. The sensor temperature (T_s) is empirically modeled using the polynomial expression in (1) [16]. The fitting parameters are found using a least squares regression on the measurements in Fig. 2 (a), assuming $T_s = T_{chuck}$. Fig. 2 (c) shows an error of less ± 0.5°C between modeled T_s and T_{Chuck} at the measured points with a standard deviation of 0.22°C.

$$T_s(I_s) = a \cdot \left(\frac{I_s}{V_s}\right)^3 + b \cdot \left(\frac{I_s}{V_s}\right)^2 + c \cdot \left(\frac{I_s}{V_s}\right) + d \qquad (1)$$

Transient measurements are performed by applying a 20 V pulse to a heater for 100 ms while measuring I_s and V_s with an oscilloscope. The current through and voltage across the heater (I_h, V_h) are also measured to calculate the instantaneous dissipated power ($P_{diss.}(t) = I_h(t) \cdot V_h(t)$). The influence of measurement noise is reduced by averaging over 64

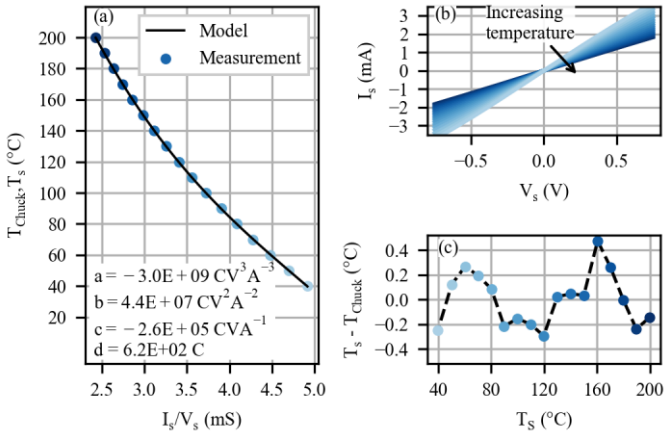

Fig. 2. (a) Chuck temperature (T_{chuck}) plotted against sensor conductivity at 0.5 V and polynomial model for sensor temperature (T_s). (b) IV-sweep on sensor for chuck temperatures from 40°C to 200°C. (c) Deviation between temperature extracted from model and chuck temperature.

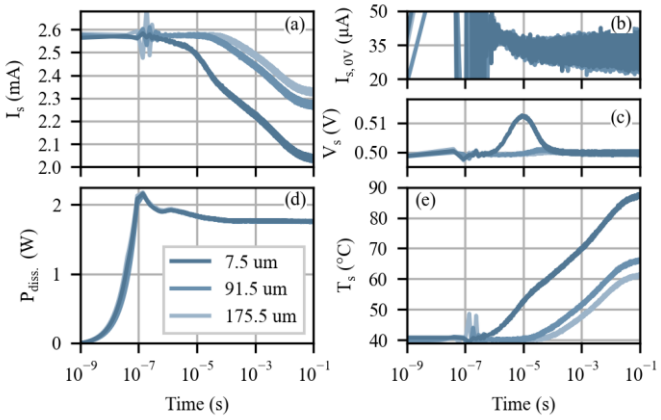

Fig. 3. Transient measurement for 7.5, 91.5 and 175.5 µm separation. (a) Sensor current, I_s. (b) 0V Sensor current, $I_{s,0V.}$ (c) Sensor voltage, V_s. (d) Dissipated power, $P_{diss.}$ (e) Sensor temperature, T_s.

acquisitions with a 1 s interval between the pulses. The result is shown in Fig. 3 for the cases with 7.5, 91.5, and 175.5 µm separation. The dissipated power is similar for all cases, with an approximately 100 ns slew rate and a 1.76 W dissipation at steady state. The change in dissipated power between 100 ns and 1 ms is attributed to self-heating and electron trapping in the heater. The bias supply is not capable of maintaining a constant V_s around 10 µs in Fig. 3 (c) when the sensor conductivity changes sharply (Fig. 3 (a)). This effect is compensated for by normalizing measured $I_s(t)$ with measured $V_s(t)$ in (1). An additional measurement is done in Fig. 3 (b), where I_s is measured while the heater is pulsed and the sensor is biased to 0 V. This measurement is used to remove an offset of 34 µA in the current probe and a systematic, dynamic change around 1 µs attributed to electrical coupling in the measurement setup. The resulting temperature increase calculated with (1) is plotted in Fig. 3 (e).

III. Numerical Model

A. Model implementation

The heat transport away from the heater is modeled with Fourier's Heat Equation,

$$\rho C_p \frac{\delta T}{\delta t} - \nabla \cdot (\kappa \nabla T) = Q \qquad (2)$$

where T is temperature, and Q is the heat generation. Further, ρ is the density, C_p is the specific heat capacity, and κ is the thermal conductivity of the material. Fourier's Heat Equation is a simplified model for the heat transport close to the heat source, but it is shown to correspond well with a more comprehensive Monte-Carlo phonon analysis at the length scales concerning coupling effects (>5 µm) [18]. The numerical model is developed to capture the primary path of heat transport from the channel of the heater to the thermal chuck, using the stack-up shown in Fig. 4. The heat transport upwards through the passivation and metallization layers is assumed to be low compared to the high thermal conductivity in the substrate and therefore not considered in the simulations to reduce complexity. The boundary of the thermal chuck is implemented as an ideal heat sink. The influence of convection and radiation effects are insignificant for the remaining boundaries, and hence, adiabatic boundary conditions are used.

COMSOL Multiphysics 3D FEM solver is used to solve (2) numerically. The heat generation Q in (2) is modeled as uniform heat flux in the 2DEG of the heater channel using a linear interpolation of the measured P_{diss}. The sensor temperature is extracted as the average temperature at the 2DEG in the sensor channel. The whole die is modeled to ensure that the influence of boundary conditions is captured in the model. The area of the heat spreader and thermal chuck is reduced to limit the computational space, ensuring that it does not influence the result. The initial temperature is set to the baseplate temperature used in the measurements. The FEM solver's mesh is designed to be dense close to the heater and sensor to capture the temperature gradients close to the heat source. The mesh density is reduced further away from the heater and sensor to reduce the computational load. The mesh is refined iteratively until further refinement gives a negligible change in the transient. The resulting mesh is shown in Fig. 5. The solver is forced to take small time steps initially to capture the fastest time constants. This is relaxed by using logarithmic time steps.

B. Material parameters

The following section discusses the choice of material parameters κ and C_p for each layer in Fig. 4, and the range within these vary. The density is chosen based on standard values for the materials from [19]. The thermal material parameters for the epitaxial layer must account for phonon scattering processes in the semiconductor material, including dislocation scattering [20]. The challenge is that these mechanisms depend on the growth and processing of the sample and, hence, are often not precisely known. The effective thermal conductivity for epitaxial GaN, κ_{GaN}, is reported to vary from 110 to 195 $Wm^{-1}K^{-1}$ at 300 K [21]. Further, the thermal conductivity exhibits a temperature dependency commonly modeled by setting it proportional to $T^{-\alpha}$, where α is fitted within a temperature interval. Typically, α between 1.0 and 1.5 is used for GaN around 300 K to 500 K. The specific heat capacity also exhibits a temperature dependency. This has been modeled with a polynomial expression in [22], which corresponds well with other reported results. The GaN layer

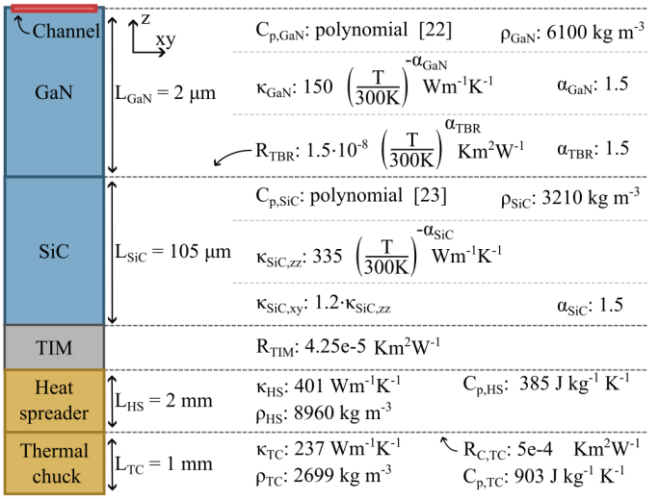

Fig. 4: Layers in numerical model with material parameters [19], [22], [23].

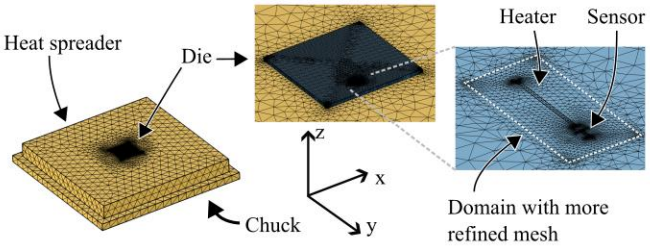

Fig. 5: Geometry in FEM solver with meshing.

thickness is unknown for the used commercial technology and must be calibrated. Typically, the thickness varies around 0.5 to 2 µm.

The heat transport in SiC is similar to that of GaN. However, the SiC crystal is additionally reported to exhibit an anisotropic thermal conductivity, which gives ≈ 20 % higher thermal conductivity in-plane (xy-axis) than out-plane (z-axis) [21]. This effect is also present for GaN but less significant. The out-plane thermal conductivity, $\kappa_{SiC,zz}$, is reported to vary around 300 to 350 $Wm^{-1}K^{-1}$ at 300K for the commonly used 4H-SiC [21]. The α value is often between 1.0 and 1.5, as with GaN, and the temperature dependency of the specific heat capacity is modeled similarly in [23]. The thickness of the SiC layer is estimated to be 105-110 µm using a dial gauge.

The nucleation layer between the epitaxial GaN and SiC substrate is reported to act as a thermal barrier resistance (TBR) varying around $5 \cdot 10^{-9}$ to $60 \cdot 10^{-9}$ Km^2W^{-1} [24]. Here, the layer is assumed to be sufficiently thin to be modeled as a single thermal resistance that takes into account heat spreading in the nucleation layer and effects at the interfaces. The temperature dependency of the TBR layer is reported with $\alpha > 2$ based on micro-Raman thermography in [24], [25]. Transient thermo-reflectance measurements in [26], [27] report the temperature dependency to be less pronounced.

The heat transport through the die attach is limited by the heat conduction in the silver epoxy and the transport across the interfaces towards the substrate and heat spreader. The model is simplified in this study by implementing the die attach as an effective thermal resistance, R_{TIM}, fitted to the measurements. This approximation assumes that the thermal capacitance and heat spreading within the silver epoxy is insignificant. The thermal conductivity of the silver epoxy is reported to be

3.9 $Wm^{-1}K^{-1}$, and the thickness is measured to be ≈ 25 µm with a dial gauge. This results in a bulk thermal resistance of ≈ $6.4 \cdot 10^{-6}$ Km^2W^{-1}. The interface resistances are expected to be in the magnitude of $1 \cdot 10^{-5}$ Km^2W^{-1} [28] and will be an important contributor to R_{TIM}.

The heat spreader is implemented with bulk values for copper at 300 K, and the thermal chuck is implemented with bulk values for aluminum at 300 K [19]. The interface resistance between the heat spreader and thermal chuck is modeled as a thermal resistance, where values around 10^{-4} to 10^{-3} Km^2W^{-1} are expected based on [29].

IV. Model Calibration

The discussion in section III.B has shown uncertainty about how the epitaxial layer, SiC substrate, and die attach layer should be implemented in the numerical model. Based on the transient measurements, this section will consider calibrating the uncertain model parameters: κ_{GaN}, R_{TBR}, L_{GaN}, κ_{SiC}, L_{SiC}, and R_{TIM}. The specific heat capacity and density are not discussed to limit the number of parameters, but the choice of these parameters could be assessed with the same approach.

A. Sensitivity analysis

First, a sensitivity analysis is done to investigate how the material parameters influence the step response. A sensitivity parameter, ζ, is defined in this study as,

$$\zeta(t) = T_s(t, \beta = \beta_0 \cdot 1.1) - T_s(t, \beta = \beta_0) \qquad (3)$$

which is the temperature change when a model parameter, denoted as β, is changed by 10% from the reference value β_0 from Fig. 4. The time derivative ζ(t), shown in Fig. 6, indicates the time region where a change to the model parameter influences the step response.

The model parameters associated with the GaN layer have an influence within the initial 100 ns to 50 µs for 7.5 µm separation. The influence of κ_{GaN} on the beginning of the transient indicates a sensitivity to the heat spreading in the GaN layer before the SiC substrate starts to influence. The thermal conductivity of the SiC substrate starts to contribute around 600 ns for 7.5 µm separation and significantly influences the temperature increase. This indicates that the heat transport through the substrate is dominant for thermal coupling with a SiC substrate. There is a sensitivity to the L_{GaN} and R_{TBR}, but it overlaps with the dominant heat spreading in the SiC substrate. While the sensitivity to R_{TBR} is low, it should be noted that it is an apparent sensitivity to the presence of the TBR layer.

The parameters associated with the heat transport in the GaN layer have a low sensitivity at 91.5 µm and 175.5 µm. Only a slight variation around the onset of the step response is seen at these separations. The sensitivity to the SiC substrate starts at the same time as a pronounced temperature increase is seen in the step response for 91.5 µm and 175.5 µm in Fig. 7. Interestingly, L_{SiC} has a similar influence on all three separations. The same is seen for the die attach layer, which has a strong sensitivity for all separations from 100 µs until a steady state is reached. The sensitivity to R_{TIM} shows that the packaging is vital to model the thermal coupling accurately.

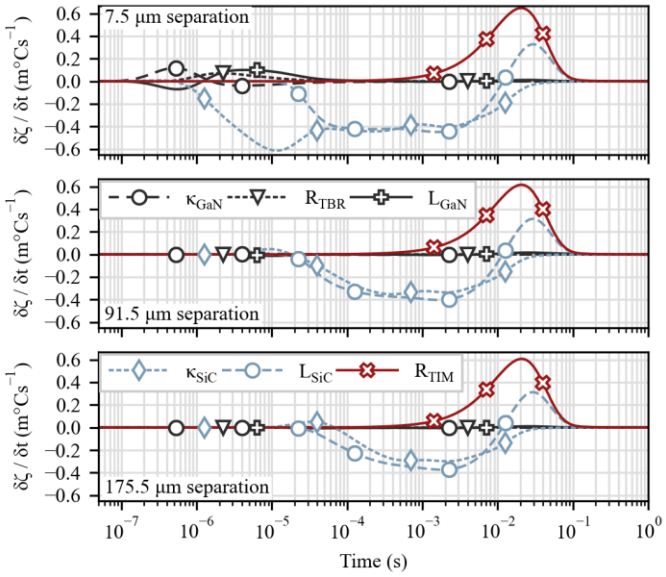

Fig. 6. Time derivative of ζ(t), defined in (3), plotted for uncertain model parameters with 7.5 µm, 91.5 µm, and 175.5 µm separation. Heat generation modeled as a Heaviside step of 1 W in the simulations.

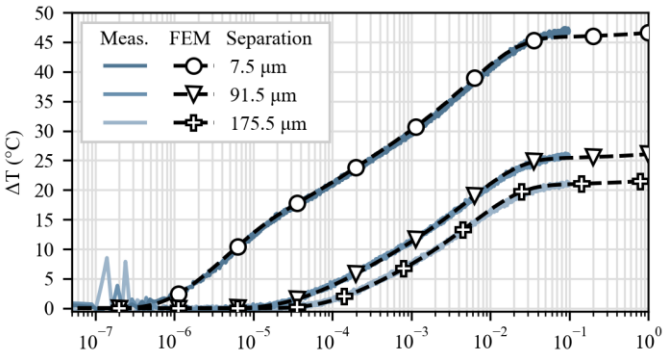

Fig. 7. Measured and simulated temperature increase for 7.5, 91.5 and 175.5 µm separation.

B. Calibration method

The sensitivity analysis has shown that each uncertain model parameter has a distinct influence on the temperature increase. The influence of the SiC substrate can be isolated by looking at the initial temperature increases at 91.5 and 175.5 µm separation, where both the epitaxial layer and die attach layer have a negligible influence. Then, the thermal resistance in the die attach layer can be fitted by looking at the time region between 1 ms and 100 ms at 91.5 and 175.5 µm separation. Next, the remaining uncertain parameters associated with the epitaxial layer can be calibrated based on the 7.5 um separation when a good fit is reached at 91.5 and 175.5 µm. This procedure allows for the separation of the contribution from the individual layers in the structure. The method can be repeated until a good fit between the model and the measurements is reached at all separations. The outlined calibration procedure has been performed to fit the uncertain model parameters to the measured temperature increase, where the chosen model parameters are found in Fig. 4. The resulting model is shown to have excellent agreement with the measured temperature increase in Fig. 7, with only some deviations are seen around 100 ms, where the heat transport in the heat spreader begins to influence.

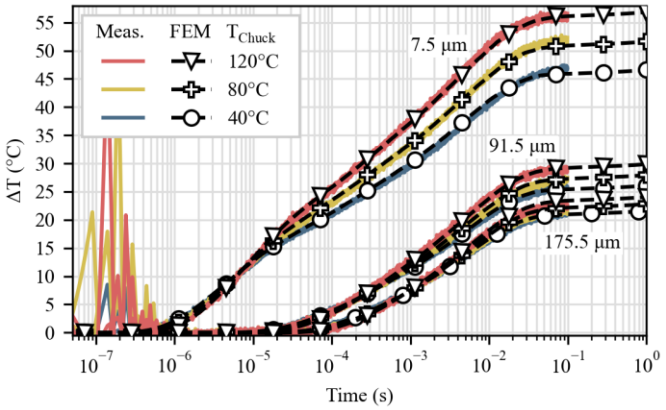

Fig. 8. Measured and simulated temperature increase for 40°C, 80°C and 120°C baseplate temperature at 7.5, 91.5, and 175.5 µm separation.

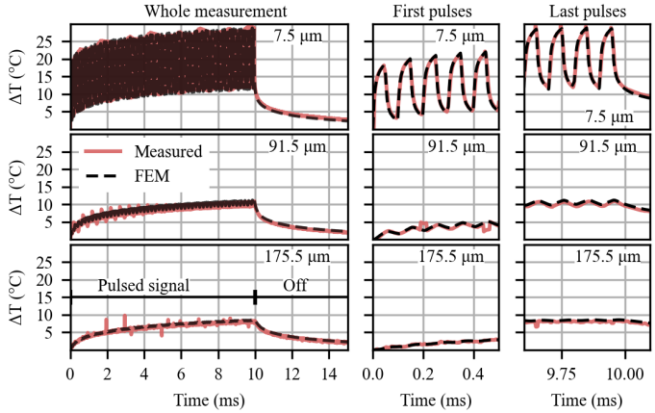

Fig. 9. Measured and simulated temperature increase at 7.5, 91.5 and 175.5 µm separation when a 50 µs pulse is applied with a 100 µs pulse repetition interval for 10 ms. Heater turned off from 10 ms to 15 ms.

C. Temperature dependency

Temperature dependency should be considered to capture the nonlinear thermal impedance due to the temperature-dependent thermal diffusivity in the semiconductor layers [11], [15]. The model has been calibrated based on the measurements in Fig. 8 with a baseplate temperature of 40°C, 80°C, and 120°C, respectively. This range represents relevant ambient operating temperatures for GaN power amplifiers. The dissipated power decreases in the measurements from a steady state $P_{diss.}$ of 1.76 W at 40°C to 1.71 W at 80°C and 1.67 W at 120°C. This is handled by changing the dissipated power in the simulations according to the measurement. The temperature dependency in the SiC substrate is fitted to α_{SiC} =1.5 based on the temperature increase at 91.5 and 175.5 µm separation, where the epitaxial layer has a negligible influence in the sensitivity analysis. The parameters in the epitaxial layers are then fitted so that the change around 5 to 50 µs is correctly modeled at 7.5 µm, using α_{GaN} = 1.5 and α_{TBR} = 1.5. The same value is used for α_{GaN} and α_{TBR} to reduce the number of fitting parameters, as they influence the response similarly. A study using transient thermoreflectance on the source field plate in [30] reported similar results with α_{SiC} = 1.55, α_{GaN} = 1.4, and α_{TBR} = 1.1. An advantage of the method proposed in this study is that it allows separation of the model parameters in the GaN layer, substrate, and die attach, while being compatible with packaged devices.

D. Validation with modulated signal

The model is assessed by applying a time-varying signal to the heater, where the heater is turned on for 50 µs with a 100 µs pulse repetition interval. Fig. 9 shows a measurement where the time-varying signal is applied for 10 ms. The measurement is continued for 5 ms after the signal is stopped. The random peaks seen at 91.5 and 175.5 µm separation are due to parasitic electrical effects in the measurements. The results show that 50 µs is sufficient time for a distinct coupling at 7.5 µm separation. The response is less distinct at 91.5 µm separation and is mainly a slow temperature increase at 175.5 µm. The temperature falls rapidly when the heater is turned off, but 50 µs is insufficient for the device to reach its initial state before the next pulse. As a result, the temperature increases gradually for each pulse until a steady state is reached over the die. The FEM simulation follows the measured response from the first to the last pulse and as the device cools down after the signal is turned off. This is achieved due to the comprehensive model implementation and the accurate calibration of model parameters. It should be noted that the FEM model is calibrated for a single device in this study, and calibration against multiple devices could be considered to capture process variations.

V. Layout Considerations

This section shows an example of how the FEM model can be used to optimize a GaN HEMTs layout. A device with four 2.5 µm x 75 µm heaters will be considered. An ungated heater is used to reuse the calibrated FEM model. This assumption neglects the influence of heat spreading from a dominant heat source next to the gate in the GaN layer for a HEMT [17]. Therefore, it does not necessarily capture the correct thermal impedance in the quasi-adiabatic region before 100 ns identified in [5]. Further, the example is simplified by not considering a source grounding via in the device layout.

First, consider the case where the four channels are placed with an equal pitch of 30 µm (Case A in Fig. 10). The simulated transient response is equal for all channels before ≈ 1µs in Fig. 10 (a). Here, the transient response overlaps with the intrinsic self-heating in the channel, as shown by a simulation with one channel. The thermal coupling from neighboring transistors adds to the intrinsic self-heating after ≈ 1 µs, and the

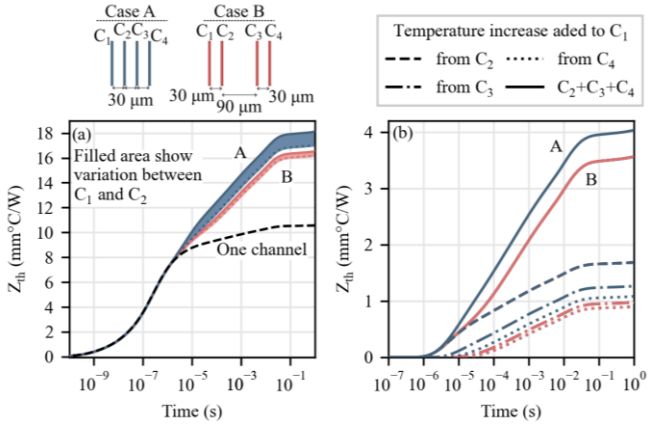

Fig. 10. Simulation with four heaters in two layouts. P_{diss} is a Heaviside step of 10 W/mm and T_0 is 40°C. (a) Transient response compared to simulation with only one channel. (b) Z_{th} added to C_1 by thermal coupling from C_2, C_3 and C_4.

thermal impedance increases compared to the simulation with one channel. This corresponds well with measured results for multichannel devices in [7]-[9]. The filled area in Fig. 10 (a) marks the temperature difference between the edge- (C_1) and center channel (C_2). Here, the edge channel has a 1.07 mm°C/W lower thermal impedance than the center channel as it, on average, is further from the other channels, and the sum of the coupling responses is lower. A more equal channel temperature can be achieved by using an unequal separation between the channels. This is done in case B, where a 90 µm separation is used between the two center channels. The increased separation gives a 1.20 mm°C/W lower average thermal impedance than case A, and the difference between C_1 and C_2 is reduced to 0.32 mm°C/W.

The effect can be understood by looking at the coupling from C_2, C_3, and C_4 added to C_1, shown in Fig. 10 (b). Both cases have the same separation between C_1 and C_2. Therefore, the sum of the coupling response is the same at the beginning of the transient. The increased separation in case B causes the contribution from C_3 and C_4 to occur later in the step response and with a lower magnitude than in case A. Hence, case B follows the contribution from C_2 longer than case A and eventually reaches a lower thermal impedance. The coupling terms in Fig. 10 (b) can explain how the thermal coupling changes the thermal impedance of a device, and this shows the added value of calibrating the FEM model based on the measured coupling response, as proposed in this article. The outlined results show the importance of thermal coupling in the thermal impedance of a HEMT. In this example, the thermal coupling increases the average thermal impedance by 7.0 and 5.8 mm°C/W for cases A and B, respectively. The configuration in cases A and B is important as they resemble the Out-Source-Via (OSV) and In-Source-Via (ISV) layouts often used in MMIC design. The results presented here correspond well with the improved electro-thermal performance of the ISV layout compared to the OSV layout [31].

For general predictions, Fig. 11 shows a contour plot of how the thermal coupling changes for increasing pitch between two channels. This coupling response is the same as shown in Fig. 10 (b) and captured in the measured results. Increasing the finger pitch reduces the magnitude of the coupling and delays the onset of the transient response. Further, the step response transitions from a fractional order response for a short pitch to become close to a first-order response for a long separation. This is consistent with the measured results here and for longer separation in [14], [32]. While the exact shape and magnitude will vary between technologies and packaging, this figure can approximate the onset and magnitude of the coupling response for a device layout.

VI. Conclusion

This article presents an accurate FEM model of dynamic thermal coupling in GaN HEMTs. The uncertain model parameters in the FEM model have been calibrated based on transient measurements with a compact temperature sensor placed 7.5, 91.5, and 175.5 µm from a heat source. Here, a method is presented for differentiating the influence of the material parameters in the epitaxial layers, substrate, and die attach layer based on a sensitivity analysis. The calibrated model shows excellent agreement with the measured self-heating for baseplate temperatures of 40°C, 80°C, and 120°C. Further, the model is accurate for a time-varying signal within the cut-off frequency of the thermal impedance.

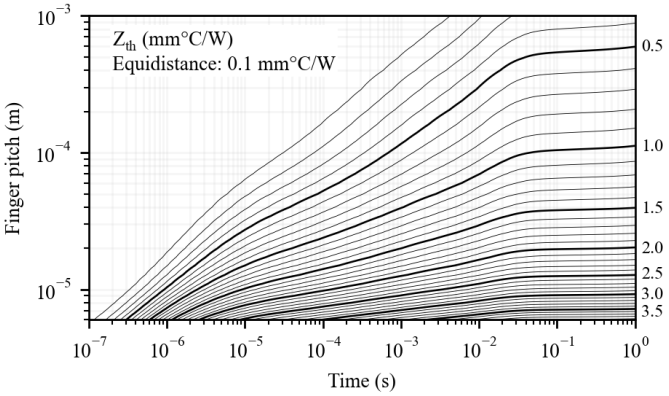

Fig. 11. Contour plot of thermal coupling response between two heaters for increasing channel pitch. P_{diss} is a Heaviside step of 10 W/mm. Z_{th} is 10.56 mm°C/W for the channel dissipating heat.

The calibrated FEM model can model how thermal coupling influences a GaN HEMTs thermal impedance. It is shown that this is valuable for optimizing device layouts. The model is not calibrated for the intrinsic heat spreading in the channel of a gated HEMT. However, it can be used to set the boundary condition for more complex models of the device physics in the channel. Further, the calibration of the GaN layer is sufficient to give a fair estimate of the average channel temperature in the HEMT and its layout dependency for electro-thermal device modeling. Finally, the method is compatible with packaged devices and can be used to evaluate different packaging solutions. The results provide new tools and guidelines for the thermal modeling of GaN HEMTs and layout optimization.

Acknowledgment

The authors would like to thank WIN Semiconductor Corp. for providing access to their NP15 process and manufacturing the test structures as a part of WIN's university multiproject wafer program.

References

[1] S. David, W. Batty, A. J. Panks, R. G. Johnson, and C. M. Snowden, "Thermal transients in microwave active devices and their influence on intermodulation distortion," *IEEE MTT-S Int. Microw. Symp. Digest*, vol. 3, pp. 431–434, 2001, doi: 10.1109/mwsym.2001.966923.

[2] J. H. K. Vuolevi, T. Rahkonen, and J. P. A. Manninen, "Measurement technique for characterizing memory effects in RF power amplifiers," *IEEE Trans. Microw. Theory Tech.*, vol. 49, no. 8, pp. 1383–1389, 2001, doi: 10.1109/22.939917.

[3] A. E. Parker and J. G. Rathmell, "Broad-band characterization of FET self-heating," *IEEE Trans. Microw. Theory Tech.*, vol. 53, no. 7, pp. 2424–2429, 2005, doi: 10.1109/TMTT.2005.850399.

[4] V. Camarchia, F. Cappelluti, M. Pirola, S. D. Guerrieri, and G. Ghione, "Self-Consistent Electrothermal Modeling of Class A, AB, and B Power GaN HEMTs Under Modulated RF Excitation," *IEEE Trans. Microw. Theory Tech.*, vol. 55, no. 9, pp. 1824–1831, 2007, doi: 10.1109/TMTT.2007.903839.

[5] G. J. Riedel, J. W. Pomeroy, K. P. Hilton, J. O. Maclean, D. J. Wallis, M. J. Uren, T. Martin, and M. Kuball, "Nanosecond timescale thermal dynamics of AlGaN/GaN electronic devices," *IEEE Electron Device Lett.*, vol. 29, no. 5, pp. 416–418, 2008, doi: 10.1109/LED.2008.919779.

[6] K. Maize, G. Pavlidis, E. Heller, L. Yates, D. Kendig, S. Graham, and A. Shakouri, "High resolution thermal characterization and simulation of

power AlGaN/GaN HEMTs using micro-Raman thermography and 800 picosecond transient thermoreflectance imaging," P*roc. IEEE Compound Semiconductor Integr. Circuit Symp., CSIC*, 2014, doi: 10.1109/CSICS.2014.6978561.

[7] A. Manoi, J. W. Pomeroy, R. Lossy, R. Pazirandeh, J. Würfl, M. J. Uren, T. Martin, and M. Kuball, "Time-dependent thermal crosstalk in multifinger AlGaN/GaN HEMTs and implications on their electrical performance," *Solid State Electron.*, vol. 57, no. 1, pp. 14–18, 2011, doi: 10.1016/j.sse.2010.11.002.

[8] A. Cutivet, G. Pavlidis, B. Hassan, M. Bouchilaoun, C. Rodriguez, A. Soltani, S. Graham, F. Boone, and H. Maher., "Scalable Modeling of Transient Self-Heating of GaN High-Electron-Mobility Transistors Based on Experimental Measurements," *IEEE Trans. Electron Devices*, vol. 66, no. 5, pp. 2139–2145, 2019, doi: 10.1109/TED.2019.2906943.

[9] B. K. Schwitter, A. E. Parker, S. J. Mahon, and M. C. Heimlich, "Characterisation of GaAs pHEMT Transient Thermal Response," *EuMIC 2018 - 2018 13th Europ. Microw. Integr. Circuits Conf.*, pp. 218–221, 2018, doi: 10.23919/EuMIC.2018.8539961.

[10] K. R. Bagnall and E. N. Wang, "Theory of Thermal Time Constants in GaN High-Electron-Mobility Transistors," *IEEE Trans. Compon. Packaging Manuf. Technol.*, vol. 8, no. 4, pp. 606–620, Apr. 2018, doi: 10.1109/TCPMT.2017.2773065.

[11] M. Kuball, S. Rajasingam, A. Sarua, M. J. Uren, T. Martin, B. T Hughes, K. P. Hilton, and R. S. Balmer , "Measurement of temperature distribution in multifinger AlGaN/GaN heterostructure field-effect transistors using micro-Raman spectroscopy," *Appl. Phys. Lett.*, vol. 82, no. 1, pp. 124–126, 2003, doi: 10.1063/1.1534935.

[12] A. Wang, L. Zeng, and W. Wang, "Three-dimensional steady and transient fully coupled electro-thermal simulation of AlGaN/GaN high electron mobility transistors: Effects of lateral heat dissipation and thermal crosstalk between gate fingers," *AIP Adv.*, vol. 7, no. 9, pp. 1–8, 2017, doi: 10.1063/1.5002544.

[13] B. K. Schwitter, A. P. Fattorini, A. E. Parker, S. J. Mahon, and M. C. Heimlich, "Parameter extractions for a GaAs pHEMT thermal model using a TFR-heated test structure," *IEEE Trans. Electron Devices*, vol. 62, no. 3, pp. 795–801, 2015, doi: 10.1109/TED.2014.2388201.

[14] J. Bremer, J. Bergsten, L. Hanning, T. M. J. Nilsson, N. Rorsman, S. Gustafsson, A. M. Eriksson, and M. Thorsell, "Analysis of Lateral Thermal Coupling for GaN MMIC Technologies," *IEEE Trans. Microw. Theory Tech.*, vol. 66, no. 10, pp. 4430–4438, 2018, doi: 10.1109/TMTT.2018.2848932.

[15] T. Kristensen, A. Divinyi, J. Bremer, T. M. J. Nilsson, and M. Thorsell, "Thermal Transient Measurements of GaN HEMT Structures by Electrical Measurements," *Proc. of the 18th Europ. Microw. Integr. Circuits Conf.*, pp. 293–296, 2023, doi: 10.23919/eumic58042.2023.10288814.

[16] A. Divinyi, T. M. J. Nilsson, N. Rorsman, T. Kristensen, H. Hultin, S. E. Gunnarsson, and M. Thorsell, "On-Chip Sensors for Temperature Monitoring of Packaged GaN MMICs," *IEEE Trans. Compon. Packaging Manuf. Technol.*, vol. PP, 2024, doi: 10.1109/TCPMT.2024.3387736.

[17] S. Rajasingam, J. W. Pomeroy, M. Kuball, M.J. Uren, T. Martin, D.C. Herbert, K.P. Hilton, and R.S. Balmer, "Micro-Raman temperature measurements for electric field assessment in active AlGaN-GaN HFETs," *IEEE Electron Device Lett.*, vol. 25, no. 7, pp. 456–458, 2004, doi: 10.1109/LED.2004.830267.

[18] Y. Shen, X. S. Chen, Y. C. Hua, H. L. Li, L. Wei, and B. Y. Cao, "Bias Dependence of Non-Fourier Heat Spreading in GaN HEMTs," *IEEE Trans. Electron Devices*, vol. 70, no. 2, pp. 409–417, 2023, doi: 10.1109/TED.2022.3227894.

[19] F. Cardarelli, *Materials Handbook : A Concise Desktop Reference.*, 3rd ed. 20. Springer International Publishing, 2018.

[20] T. Wang, J. Carrete, N. Mingo, and G. K. H. Madsen, "Phonon Scattering by Dislocations in GaN," *ACS Appl Mater Interfaces*, vol. 11, no. 8, pp. 8175–8181, 2019, doi: 10.1021/acsami.8b17525.

[21] Q. Zheng, C. Li, A. Rai, J. H. Leach, D. A. Broido, and D. G. Cahill, "Thermal conductivity of GaN, GaN 71, and SiC from 150 K to 850 K," *Phys. Rev. Mater.*, vol. 3, no. 1, 2019, doi: 10.1103/PhysRevMaterials.3.014601.

[22] S. Lee, S. Y. Kwon, and H. J. Ham, "Specific heat capacity of gallium nitride," *Jpn. J. Appl. Phys.*, vol. 50, no. 11 PART 2, pp. 8–11, 2011, doi: 10.1143/JJAP.50.11RG02.

[23] L. Hitova, R. Yakimova, E. P. Trifonova, A. Lenchev, and E. Janzen, "Heat Capacity of 4H-SiC Determined by Differential Scanning Calorimetry," *J. Electrochem. Soc.*, vol. 147, no. 9, p. 3546, 2000, doi: 10.1149/1.1393935.

[24] A. Manoi, J. W. Pomeroy, N. Killat, and M. Kuball, "Benchmarking of Thermal Boundary Resistance in AlGaN/GaN HEMTs on SiC Substrates: Implications of the Nucleation Layer Microstructure," *IEEE Electron Device Lett.*, vol. 31, no. 12, pp. 1395–1397, Dec. 2010, doi: 10.1109/LED.2010.2077730.

[25] A. Sarua, H. Ji, K.P. Hilton, D. J. Wallis, M. J. Uren, T. Martin, and M. Kuball, "Thermal boundary resistance between GaN and substrate in AlGaN/GaN electronic devices," *IEEE Trans. Electron Devices*, vol. 54, no. 12, pp. 3152–3158, 2007, doi: 10.1109/TED.2007.908874.

[26] J. Cho, Y. Li, W. E. Hoke, D. H. Altman, M. Asheghi, and K. E. Goodson, "Phonon scattering in strained transition layers for GaN heteroepitaxy," *Phys. Rev. B Condens. Matter Mater Phys.*, vol. 89, no. 11, pp. 1–11, 2014, doi: 10.1103/PhysRevB.89.115301.

[27] C. Yuan, J. W. Pomeroy, and M. Kuball, "Non-invasive Thermal Resistance Measurement for GaN Wafer Process Control and Optimization," *Proc. of the 17th Intersoc. Conf. Therm. Thermomech. Phenomena Electronic Syst. (ITherm) 2018*, pp. 256–261, 2018, doi: 10.1109/ITHERM.2018.8419633.

[28] G. Gao, D. Li, J. J. Gou, C. L. Gong, and S. M. Li, "The quantitative study of interfacial contact effects in TEGs by real-topology-based simulations and novel indirect tests," *Int. J. Heat Mass Transf.*, vol. 201, p. 123579, 2023, doi: 10.1016/j.ijheatmasstransfer.2022.123579.

[29] J. W. Zhao, R. Zhao, Y. K. Huo, and W. L. Cheng, "Effects of surface roughness, temperature and pressure on interface thermal resistance of thermal interface materials," *Int. J Heat Mass. Transf.*, vol. 140, pp. 705–716, 2019, doi: 10.1016/j.ijheatmasstransfer.2019.06.045.

[30] X. Zheng, J. W. Pomeroy, G. Jindal, and M. Kuball, "Temperature-Dependent Thermal Impedance Measurement of GaN-Based HEMTs Using Transient Thermoreflectance," *IEEE Trans. Electron Devices*, vol. PP, pp. 1–6, 2024, doi: 10.1109/TED.2024.3367309.

[31] Y. N. Zhong and Y. M. Hsin, "Thermal analysis of GaN-on-SiC HEMTs with different backside via layouts," *Jpn. J. Appl. Phys.*, vol. 58, no. SC, 2019, doi: 10.7567/1347-4065/ab12c6.

[32] T. Kristensen, T. M. J. Nilsson, A. Divinyi, J. Bremer, and M. Thorsell, "Characterization and Modeling of Dynamic Thermal Coupling in GaN MMIC Power Amplifiers," *2024 IEEE/MTT-S Int. Microw. Symp. -IMS 2024*, Washington, DC, USA 2024, pp. 1053-1056, doi: 10.1109/IMS40175.2024.10600290.